

## Research Article

# Photothermal Effect of Superparamagnetic Fe<sub>3</sub>O<sub>4</sub> Nanoparticles Irradiated by Near-Infrared Laser

Shawei Fu , Yuchun Man, and Fuquan Jia

*Inorganic Synthesis and Chemical Analysis Institute, Jilin Architectural University, Changchun, Jilin Province, China 130118*

Correspondence should be addressed to Shawei Fu; [fuswmm@163.com](mailto:fuswmm@163.com)

Received 13 July 2020; Accepted 3 August 2020; Published 14 October 2020

Guest Editor: Zhenyi Zhang

Copyright © 2020 Shawei Fu et al. This is an open access article distributed under the Creative Commons Attribution License, which permits unrestricted use, distribution, and reproduction in any medium, provided the original work is properly cited.

Fe<sub>3</sub>O<sub>4</sub> nanoparticles (NPs) have been widely used in biomedicine due to their unique magnetism, biocompatibility, and biodegradability. Magnetic hyperthermia of Fe<sub>3</sub>O<sub>4</sub> NPs for cancer treatment has attracted more attention. However, it could interfere with magnetic field-sensitive devices of patients, such as pacemakers. Therefore, it is necessary to find a new method for clinical therapy. In this study, the superparamagnetic Fe<sub>3</sub>O<sub>4</sub> NPs were fabricated. Visible-near-infrared absorption spectra indicated that the Fe<sub>3</sub>O<sub>4</sub> NPs have near-infrared absorption. The influences of Fe<sub>3</sub>O<sub>4</sub> NP concentrations, power density, and wavelength of near-infrared laser irradiation on the photothermal performance of Fe<sub>3</sub>O<sub>4</sub> NPs were investigated. The results revealed that high concentrations, large power density, and short irradiation wavelength could improve the photothermal performance of Fe<sub>3</sub>O<sub>4</sub> NPs. The temperature variation and the absorption intensity simultaneously determined the photothermal transduction efficiency of Fe<sub>3</sub>O<sub>4</sub> NPs. The application of the photothermal performance of Fe<sub>3</sub>O<sub>4</sub> NPs would provide a new opportunity for clinic cancer treatment.

## 1. Introduction

In recent years, nanomaterials have been widely used in photocatalysis [1–3] and electrochemical applications [4]. With recent nanotechnology developments, more and more nanomaterials find their practical as well as potential applications in biomedicine [5–9]. One of such example is the application of superparamagnetic Fe<sub>3</sub>O<sub>4</sub> NPs for cell targeting, drug delivery, magnetic resonance imaging, and magnetic hyperthermal cancer therapy, all of which rely on unique magnetic properties of Fe<sub>3</sub>O<sub>4</sub> as well as its biocompatibility and biodegradability [10–14]. Specially designed Fe<sub>3</sub>O<sub>4</sub> NPs and their composites demonstrating diverse performance characteristics are promising prospects for theranostic applications [15–19]. However, using magnetic hyperthermia for cancer treatment might not be applicable to a wide-enough extent. For example, patients with implanted devices sensitive to magnetic fields (e.g., pacemakers) cannot be treated by the external magnetic field [20]. High-intensity magnetic fields might bring other potential risks to patients.

Photothermal therapy (PTT) recently emerged as a promising strategy to battle cancer [21–24]. It uses photo-

thermal agents to ablate cancer cells in combination with near-infrared (NIR) irradiation to raise local temperature around the tumour. Comparing with magnetic hyperthermal therapy, PTT is more convenient and safer. Heat generated from photothermal nanoagents irradiated by a laser is directed exactly and precisely at the cancer cells, which significantly reduces potential damage to surrounding healthy cells and tissues. Ideal PTT agents not only absorb NIR but also have high photothermal conversion efficiency. Numerous PTT agents were extensively studied by other research groups, such as noble metals (Au and Ag), carbon-based material, and polymers [25]. All of these agents can absorb NIR irradiation and convert it into heat.

Fe<sub>3</sub>O<sub>4</sub> NPs absorb light in a wider range: from the visible to the NIR part of the light spectrum. The energy absorption of Fe<sub>3</sub>O<sub>4</sub> NPs in the NIR region can be exploited. In addition, electron nonradiative transition of Fe<sub>3</sub>O<sub>4</sub> NPs in the NIR region also releases thermal energy. The absorption at the NIR region of Fe<sub>3</sub>O<sub>4</sub> NPs is attributed to the indirect band gap transition of Fe(III) 3d electrons. The electronic transitions may contribute to the absorption of Fe<sub>3</sub>O<sub>4</sub>, namely, d-d transitions of the Fe(II) and Fe(III) ions in the visible-

NIR wavelength range [11, 26]. Thus,  $\text{Fe}_3\text{O}_4$  NPs might become next-generation photothermal agents for cancer therapy. At present, a lot of effort was dedicated to combine  $\text{Fe}_3\text{O}_4$  NPs with other photothermal agents to achieve photothermal cancer therapy [10, 15, 23, 27]. In these nanocomposites,  $\text{Fe}_3\text{O}_4$  was only implemented to enhance magnetic targeting and imaging of the composite. The photothermal effect of  $\text{Fe}_3\text{O}_4$  NPs was not considered at all. However, we believe that individual  $\text{Fe}_3\text{O}_4$  NPs acting as photothermal agents could simultaneously achieve multiple functions, which will help to avoid complex preparation of composites for cancer therapy. Another very important aspect is superior biosafety of  $\text{Fe}_3\text{O}_4$  NPs in comparison to other photothermal agents [28].  $\text{Fe}_3\text{O}_4$  NPs have excellent biocompatibility and can be easily excreted from the body.

In this work,  $\text{Fe}_3\text{O}_4$  NPs were fabricated by the thermal decomposition method, after which water soluble nanocrystals were obtained using the surface ligand exchange technique. Photothermal performance of the  $\text{Fe}_3\text{O}_4$  NPs was studied.  $\text{Fe}_3\text{O}_4$  NPs were used for magnetic targeting photothermal therapy against cancer cells using NIR irradiation.

## 2. Materials and Methods

**2.1. Initial Chemicals.** All initial compounds were analytically pure and used without any further treatment. We purchased 1,2-hexadecanediol (90% pure), iron acetylacetonate ( $\text{Fe}(\text{acac})_3$ , 99.9% pure), benzyl ether (99% pure), oleylamine (OLA, 70% pure), branched polyethylenimine (PEI, 25000 kDa), oleic acid (OA, 90% pure), and chloroform from Sigma Chemical Company (USA). Hexyl hydride was obtained from Sinopharm Chemical Reagent (China).

**2.2. Synthesis.**  $\text{Fe}_3\text{O}_4$  NPs were synthesized using the thermal decomposition technique [29]. For this purpose, 2 mmol of  $\text{Fe}(\text{acac})_3$ , 10 mmol of 1,2-hexadecanediol, and 6 mmol of OA and OLA were mixed in 20 mL of benzyl ether in a three-neck flask. The resulting solution was stirred under  $\text{N}_2$  atmosphere. The solution was heated to 200°C and kept at this temperature for 30 min, after which it was heated to 300°C and refluxed for 1 h. The resulting solution was gradually cooled to room temperature.  $\text{Fe}_3\text{O}_4$  NPs were rinsed with ethanol several times and then suspended in chloroform. 0.004 mM  $\text{Fe}_3\text{O}_4$ -chloroform suspension was then diluted again in 1 mM PEI-chloroform solution under constant stirring at room temperature. After 48 h, hexyl hydride was added into the suspension. The final product was PEI-capped  $\text{Fe}_3\text{O}_4$  precipitates, which were washed three times with water and then dispersed in deionized water.

**2.3. Photothermal Tests.**  $\text{Fe}_3\text{O}_4$  NP suspensions with different concentrations were placed into centrifuge tubes. These suspensions were then irradiated by lasers with different power densities. Temperatures of these suspensions were recorded every minute for 15 consecutive minutes. We also irradiated  $\text{Fe}_3\text{O}_4$  NPs that were placed in a thin plastic bag using a similar empty bag as a reference.

**2.4. Cytotoxicity Assay.** Cells of 4T1 mouse breast cancer cells were cultured at 37°C in 5%  $\text{CO}_2$  atmosphere using

RPMI-1640 as a medium with addition of fetal bovine serum (10%), streptomycin (100  $\mu\text{g}/\text{mL}$ ), and penicillin (100 U/mL). Prior to the assay, 4T1 cells were seeded in a 96-well plate ( $10^4$  cells/well) for 12 h, after which  $\text{Fe}_3\text{O}_4$  NPs with different concentrations were added to each well. Cultivation was performed at 37°C for 24 h, after which 20  $\mu\text{L}$  of 5 mg/mL methyl thiazolyl tetrazolium (MTT) was added, and the cells were incubated for another 4 h. MTT assay was performed to determine cell viabilities (relative to the control), which was expressed as a percentage of the control. The final value represents an average one. The measurement error represents standard deviation (SD).

**2.5. Photothermal Treatment of Breast Cancer 4T1 Cells.** 4T1 cells were incubated with 0.1 mg/mL  $\text{Fe}_3\text{O}_4$  NPs at 37°C for 1 h. After the treatment, excess  $\text{Fe}_3\text{O}_4$  was removed by rinsing with phosphate buffer saline, after which a standard MTT assay (performed as described above) was implemented to examine how  $\text{Fe}_3\text{O}_4$  presence affected 4T1 cells. Another series of 4T1 cells after incubation was irradiated by an 808 nm laser for 10 min with 1 W/cm<sup>2</sup> power density with or without an applied magnetic field. After the irradiation, cell viability was also analyzed by MTT assay.

**2.6. Characterization.** Micromorphologies of the resulting samples were obtained by transmission electron microscopy (TEM) using an FEI Tecnai G2 S-Twin. Phase compositions as well as their crystallinity degree were determined by X-ray diffraction (XRD) using a D/MAX-RA XRD Rigaku system with  $\text{Cu K}\alpha$  radiation at 50 kV and 300 mA operating voltage and current, respectively. Effect of the magnetic field on the samples was obtained at 300 K using an MPMS-XL-5 SQUID magnetometer. The magnetic field was cycled between -30 and +30 kOe. UV-vis-near-IR absorption spectra were recorded using a PerkinElmer UV WinLab spectrophotometer.

## 3. Results and Discussion

TEM analysis showed uniform monodispersed  $\text{Fe}_3\text{O}_4$  NPs (see Figure 1(a))  $5.5 \pm 0.5$  nm in diameter. XRD analysis confirmed that the resulting NPs were pure  $\text{Fe}_3\text{O}_4$  with a cubic inverse spinel structure (according to JCPDS 75-1610), as shown in Figure 1(b).

Magnetic properties  $\text{Fe}_3\text{O}_4$  NPs were obtained using a field-dependent magnetization technique. Hysteresis loop of  $\text{Fe}_3\text{O}_4$  NPs at room temperature showed no hysteresis; thus, our resulting  $\text{Fe}_3\text{O}_4$  NPs were superparamagnetic (see Figure 2(a)). Saturation magnetization of  $\text{Fe}_3\text{O}_4$  NPs was ~39.5 emu/g, which indicates strong magnetism. Figure 2(b) shows  $\text{Fe}_3\text{O}_4$  NPs in an aqueous solution with and without application of an external magnetic field. When suspended  $\text{Fe}_3\text{O}_4$  NPs were not subjected to the magnetic field, they were well-dispersed and suitable for biological applications. When a magnet was in contact with one side of the vial,  $\text{Fe}_3\text{O}_4$  NPs quickly separated from the aqueous solution and attached to the vial wall near the magnet. As a result, the solution became clear.

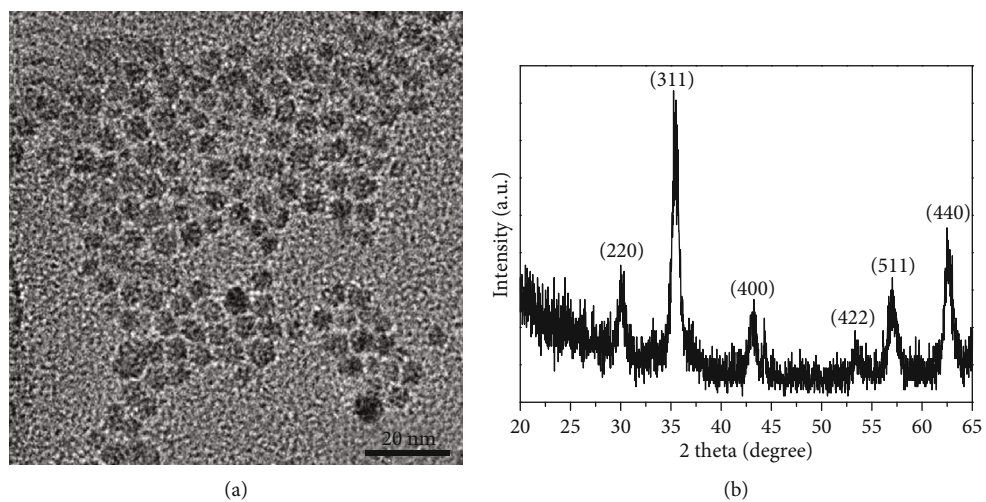


FIGURE 1: (a) TEM micrographs and (b) XRD patterns of  $\text{Fe}_3\text{O}_4$  NPs.

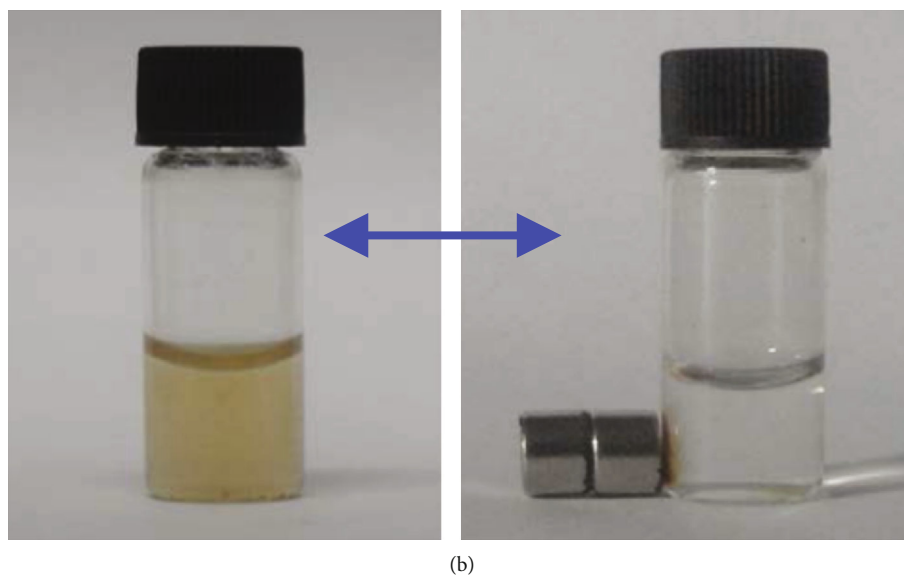
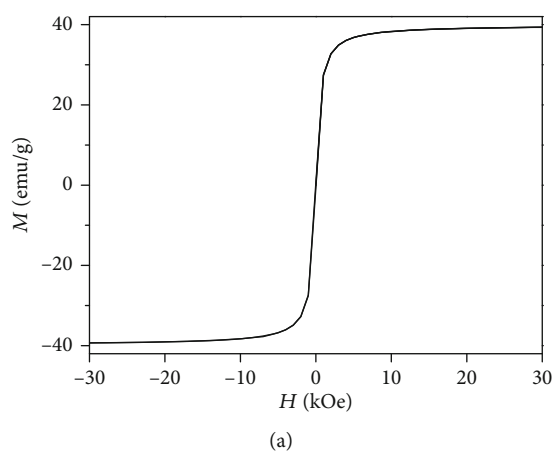


FIGURE 2: (a) Magnetic hysteresis loop and (b) left-hand-side photograph of  $\text{Fe}_3\text{O}_4$  NPs suspended in water under daylight. Right-hand-side photograph shows a magnet in contact with the wall of the vial. The solution became clear because all  $\text{Fe}_3\text{O}_4$  NPs were attracted by the magnet and separated from the water.

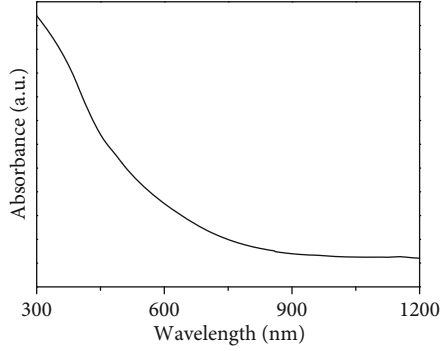


FIGURE 3: Absorption spectra of  $\text{Fe}_3\text{O}_4$  NPs in the 400-1000 nm region.

The absorption spectrum of the 0.1 mg/mL suspension of  $\text{Fe}_3\text{O}_4$  NPs showed higher absorption intensity in the visible region than in the NIR region (see Figure 3). However, the penetrability of visible light is not strong; it was not to be used for biomedical applications. Although the absorption intensity in the NIR region is not as strong as that in the visible region, it is enough to produce excellent photothermal performance, as shown in the following photothermal test.

Photothermal performance of  $\text{Fe}_3\text{O}_4$  NPs was tested by measuring the temperature of aqueous suspensions containing different contents of  $\text{Fe}_3\text{O}_4$  NPs. These suspensions were irradiated using different laser power densities and wavelengths (see Figure 4). When the suspensions were irradiated by an 808 nm laser, higher temperatures were observed in suspensions with higher  $\text{Fe}_3\text{O}_4$  NPs contents (see Figure 4(a)). For example, when a suspension containing 0.05 mg/mL of  $\text{Fe}_3\text{O}_4$  NPs was irradiated by an 808 nm laser for 10 min, temperature increased 29.4°C. However, in the case of 1 mg/mL  $\text{Fe}_3\text{O}_4$  NP suspensions, laser irradiation increased suspension temperature by 46.3°C. More significant temperature increase for suspensions with higher  $\text{Fe}_3\text{O}_4$  NP contents was attributed to more absorbed irradiation (because there were more particles in the suspension), which was then converted into heat. Our control experiments with aqueous solutions containing no  $\text{Fe}_3\text{O}_4$  NPs showed only up to 4.4°C temperature increase upon the same laser irradiation conditions.

Laser power density also affected temperature increase. Laser power density equal to 0.4 W/cm<sup>2</sup> was not enough to produce significantly increased temperature of  $\text{Fe}_3\text{O}_4$  NP suspensions (see Figure 4(b)). Temperatures of the 0.1 mg/mL  $\text{Fe}_3\text{O}_4$  NP suspension upon its 10 min irradiation with an 808 nm laser at 1 and 2 W/cm<sup>2</sup> power densities were increased 33.9 and 46.1°C, respectively.

We also studied temperature changes of  $\text{Fe}_3\text{O}_4$  NP suspensions upon their irradiation by lasers with different wavelengths (see Figure 4(c)). Irradiation by lasers with shorter wavelengths increased suspension temperatures more than irradiation with laser with longer wavelengths, which corresponds to the results of our light-absorption experiments: more energy was absorbed in the visible part of the spectrum than in the NIR. However, the main reason of popularity of photothermal treatments using NIR irradiation for biomed-

cal applications is its strong penetrability into the tissues and biological/physiological systems.

Photothermal conversion efficiency is an important parameter to evaluate the photothermal properties of materials. To calculate the photothermal conversion efficiency of  $\text{Fe}_3\text{O}_4$  NPs, an energy balance on the system is required [18, 26, 30]. The total energy balance for the system is

$$Q_{\text{Mater}} + Q_0 - Q_{\text{output}} = \sum m_i c_{p,i} \frac{dT}{dt}, \quad (1)$$

where  $Q_{\text{Mater}}$  is the heat generated by the material under laser irradiation,  $Q_0$  is the heat generated by water under laser irradiation,  $Q_{\text{output}}$  is the heat transferred from the system to the environment,  $m_i$  is the mass, and  $C_{p,i}$  is the heat capacity.

$$Q_{\text{Mater}} = P(1 - 10^{-A_\lambda})\eta, \quad (2)$$

$$\eta = \frac{Q_{\text{Mater}}}{P(1 - 10^{-A_\lambda})},$$

where  $P$  is the laser power,  $A_\lambda$  is the absorption intensity at the excitation wavelength of  $\lambda$  (nm), and  $\eta$  is the photothermal conversion efficiency.

$$Q_{\text{output}} = hs(T - T_{\text{surr}}), \quad (3)$$

where  $h$  is the heat transfer coefficient,  $s$  is the surface area of the container,  $T$  is the solution temperature, and  $T_{\text{surr}}$  is the ambient surrounding temperature. In order to calculate  $hs$ , the cooling stage is studied. After removing the laser excitation, the heat generated by the system is stopped. Equation (1) becomes

$$\sum m_i c_{p,i} \frac{dT}{dt} = -Q_{\text{output}} = -hs(T - T_{\text{surr}}). \quad (4)$$

Rearranging Equation (3)

$$dt = -\frac{\sum m_i c_{p,i}}{hs} \frac{dT}{(T - T_{\text{surr}})}, \quad (5)$$

then integrating

$$t = -\frac{\sum m_i c_{p,i}}{hs} \ln(T - T_{\text{surr}}) + b. \quad (6)$$

Let  $\tau_0$  be the time constant for heat transfer from the system

$$\tau_0 = \frac{\sum m_i c_{p,i}}{hs}. \quad (7)$$

During solution cooling, the temperature decrease was monitored.  $\tau_0$  is calculated according to the temperature changes of the solution as a function of time. Thus,  $hs$  can be computed.

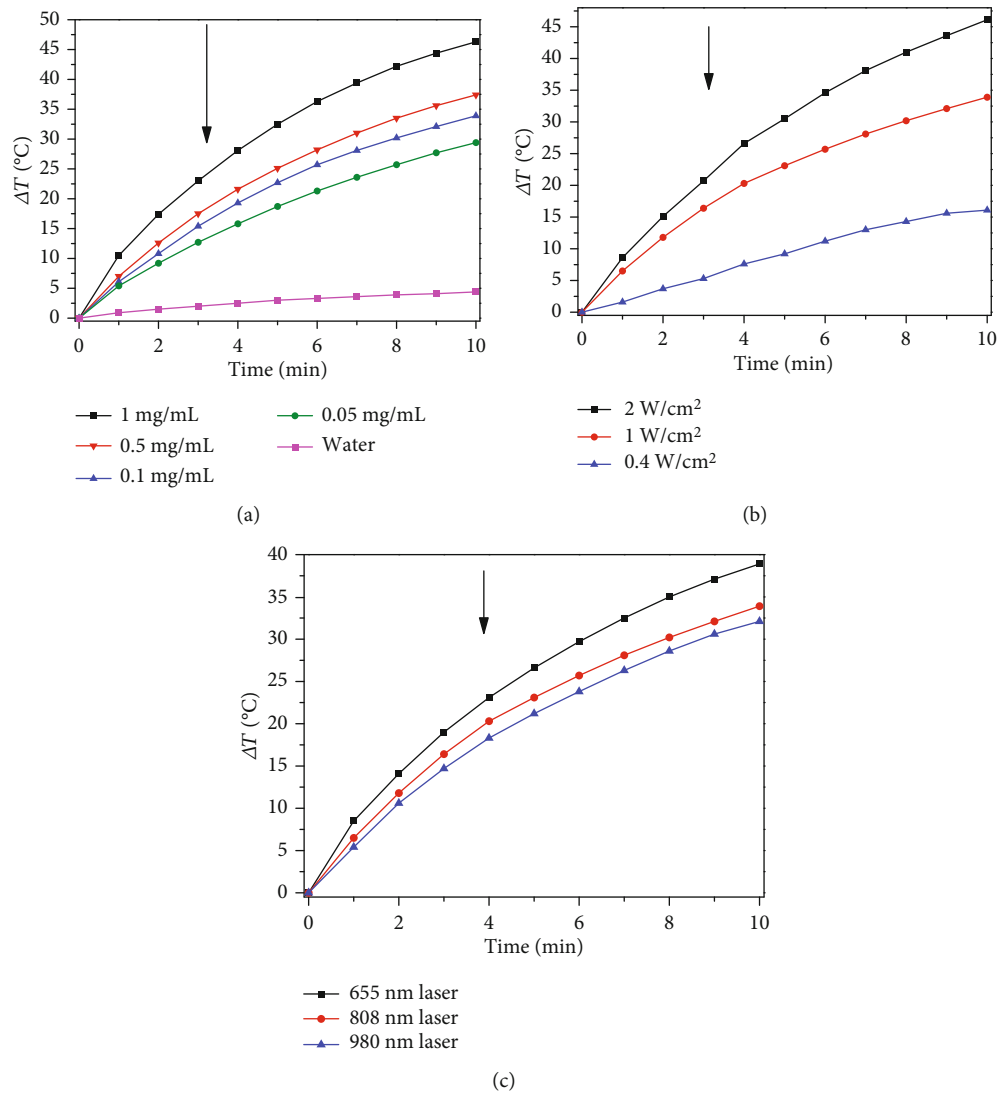


FIGURE 4: (a) Temperature increase of  $\text{Fe}_3\text{O}_4$  NP suspensions with different concentrations (laser wavelength: 808 nm, laser power density:  $1 \text{ W/cm}^2$ ). (b) Irradiated by a laser with different power densities (concentration:  $0.1 \text{ mg/mL}$ , laser wavelength: 808 nm) and (c) irradiated by lasers with different wavelengths (concentration:  $0.1 \text{ mg/mL}$ , laser power density:  $1 \text{ W/cm}^2$ ).

At the maximum steady-state temperature, the heat transfer between the system and the environment reaches equilibrium. The temperature is a constant.

$$\frac{dT}{dt} = 0. \quad (8)$$

Equation (1) gives the expression

$$Q_{\text{Mater}} = Q_{\text{output}} - Q_0. \quad (9)$$

Then, Equations (3) and (4) give the expression

$$\eta = \frac{hs(T - T_{\text{surr}}) - Q_0}{P(1 - 10^{-A_\lambda})}. \quad (10)$$

In order to further study the photothermal performance of the  $\text{Fe}_3\text{O}_4$  NPs, we recorded the temperature change of the  $1 \text{ mL}$   $\text{Fe}_3\text{O}_4$  NP suspensions at different concentrations as a function of time under continuous different power densities of the 808 nm laser irradiation until the suspensions reached a steady-state temperature. Then, the laser was turned off and the suspension was cooled (see Figure 5(a)). The linear time data versus negative natural logarithm of the temperature driving force is obtained by the cooling process as shown in Figures 5(b)–5(d). According to the obtained data, the time constant of  $0.1 \text{ mg/mL}$   $\text{Fe}_3\text{O}_4$  NP suspensions with an 808 nm laser irradiation at  $2 \text{ W/cm}^2$  power densities is determined to be  $\tau_0 = 559.3 \text{ s}$ . The time constant of  $0.5 \text{ mg/mL}$   $\text{Fe}_3\text{O}_4$  NP suspensions with an 808 nm laser irradiation at  $1 \text{ W/cm}^2$  power densities is determined to be  $\tau_0 = 487.3 \text{ s}$ . The time constant of  $0.1 \text{ mg/mL}$   $\text{Fe}_3\text{O}_4$  NP suspensions with an 808 nm laser irradiation at  $1 \text{ W/cm}^2$  power

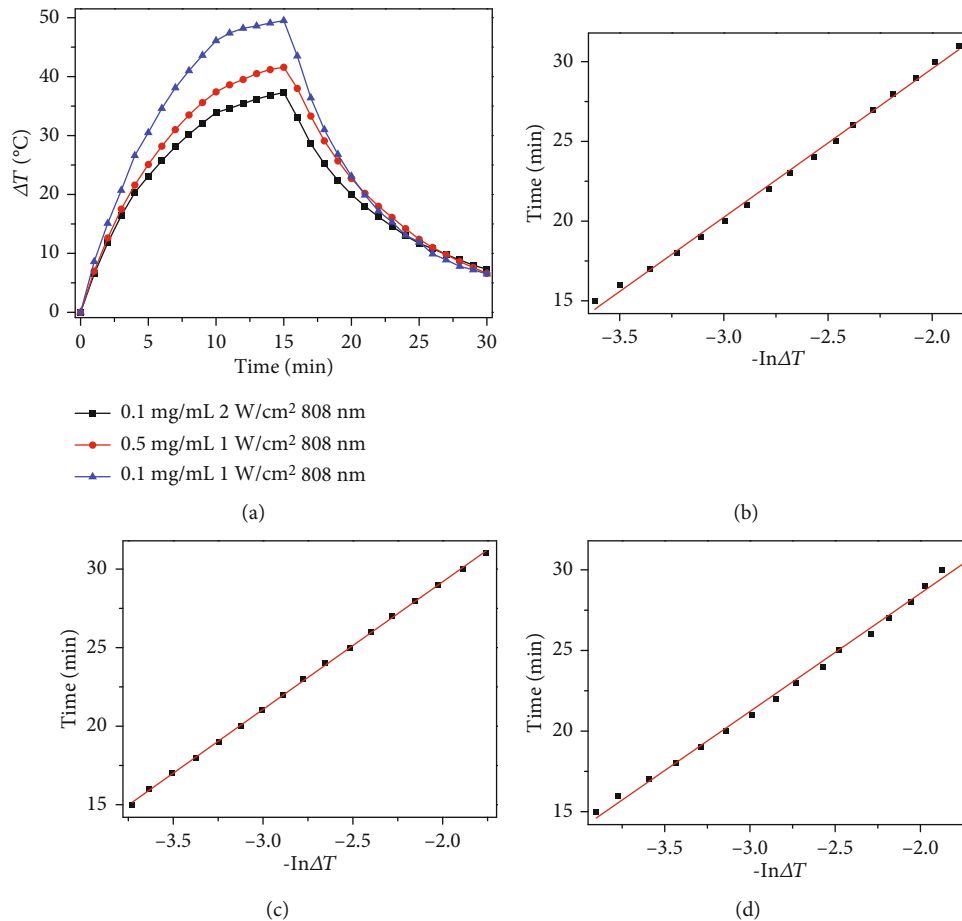


FIGURE 5: (a) Photothermal effect of the irradiation of Fe<sub>3</sub>O<sub>4</sub> NP suspensions with an 808 nm laser. The suspension is irradiated for 15 min and cooled to room temperature under ambient environment. (b–d) Plot of cooling time versus negative natural logarithm of the temperature driving force obtained from the cooling stage.

densities is determined to be  $\tau_0 = 439.5$  s. According to Equations (7) and (10), the relevant parameters are inputted into the formula. The photothermal conversion efficiency is about 2.23%, 4.64%, and 6.57%, respectively. It can be seen that the photothermal performance of NPs is not only contributed by absorption, but also determined by photothermal conversion efficiency.

The mouse 4T1 breast cancer cells were selected to investigate the toxicity of Fe<sub>3</sub>O<sub>4</sub> NPs by standard MTT assay. The 4T1 cells were incubated with different mass concentrations of the Fe<sub>3</sub>O<sub>4</sub> NP suspension at 37 $^{\circ}\text{C}$  for 24 h. As displayed in Figure 6, the viability of cancer cells was about 97.6% when the concentration of the Fe<sub>3</sub>O<sub>4</sub> NP suspension was 0.01 mg/mL. With the increase of the Fe<sub>3</sub>O<sub>4</sub> NP concentration, the viabilities of cancer cells were gradually decreased. But even when the concentration of the Fe<sub>3</sub>O<sub>4</sub> NP suspension was 1 mg/mL, the viabilities of cancer cells were still about 94.1%. It indicates the low cellular toxicity of the Fe<sub>3</sub>O<sub>4</sub> NPs.

To demonstrate the photothermal effect of Fe<sub>3</sub>O<sub>4</sub> NP suspensions for cancer treatment, we used mouse 4T1 breast cancer cells (see Figure 7). The cells with the 808 nm laser irradiation at the power density of 1 W/cm<sup>2</sup> or 2 W/cm<sup>2</sup> for 10 min had no significant cellular death.

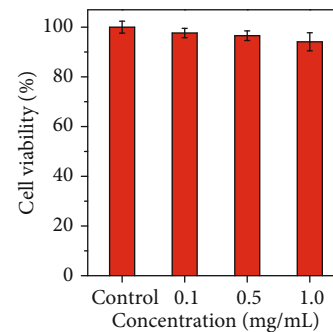


FIGURE 6: Cytotoxicity of Fe<sub>3</sub>O<sub>4</sub> NPs with different concentrations.

As discussed above, the Fe<sub>3</sub>O<sub>4</sub> NPs of 0.1 mg/mL have little cellular toxicity. However, after the 808 nm laser irradiation at the power density of 1 W/cm<sup>2</sup> for 10 min, the cell viability reduced to 50.5% for 4T1 cells incubated with Fe<sub>3</sub>O<sub>4</sub> NPs. It reduced even more after application of an external magnetic field. Under the external magnetic field, the viability further reduced to 24.1% for the cells incubated with Fe<sub>3</sub>O<sub>4</sub> NPs. Thus, application of a magnetic field significantly enhanced the photothermal effect of Fe<sub>3</sub>O<sub>4</sub> NPs.

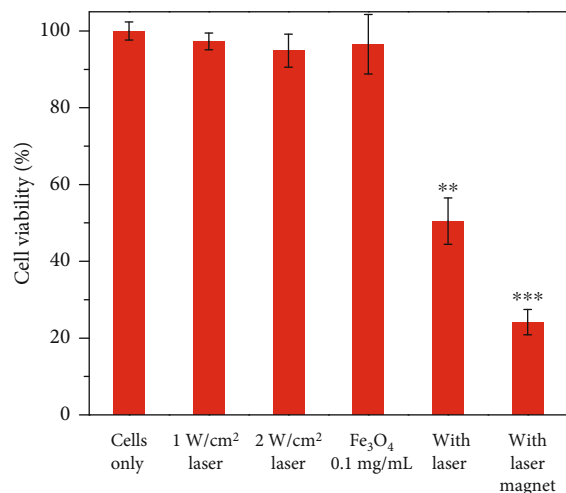


FIGURE 7: Viability of 4T1 cancer cells treated by combination of Fe<sub>3</sub>O<sub>4</sub> NPs with and without an 808 nm laser irradiation and with and without application of an external magnetic field. Error bars represent standard deviations, \*\* $p < 0.01$ , and \*\*\* $p < 0.001$ .

#### 4. Conclusions

We successfully prepared superparamagnetic Fe<sub>3</sub>O<sub>4</sub> NPs by the thermal decomposition method. These Fe<sub>3</sub>O<sub>4</sub> NPs demonstrated absorption in both the visible and NIR spectra and were able to convert light energy into heat. High concentration of Fe<sub>3</sub>O<sub>4</sub> NPs in an aqueous suspension and high power density as well as shorter wavelengths of a laser resulted in a significantly more enhanced photothermal effect of Fe<sub>3</sub>O<sub>4</sub> NPs. Photothermal destruction of cancer cells had the best efficiency when it was performed with the application of an external magnetic field.

#### Data Availability

All data used to support the findings of this study are included within the article.

#### Conflicts of Interest

The authors declare that there is no conflict of interest regarding the publication of this paper.

#### Acknowledgments

This work was supported by the Jilin Provincial Education Department “13th Five-Year” Science and Technology Research Planning Project (JJKH20180584KJ).

#### References

- [1] P. Zhang, S. Zhang, D. Wan, P. Zhang, Z. Zhang, and G. Shao, “Multilevel polarization-fields enhanced capture and photocatalytic conversion of particulate matter over flexible Schottky-junction nanofiber membranes,” *Journal of Hazardous Materials*, vol. 395, article 122639, 2020.
- [2] M. Zhang, Y. Qi, and Z. Zhang, “AgBr/BiOBr nano-heterostructure-decorated polyacrylonitrile nanofibers: a recyclable high-performance photocatalyst for dye degradation under visible-light irradiation,” *Polymers*, vol. 11, no. 10, p. 1718, 2019.
- [3] D. Dong, C. Yan, J. Huang et al., “An electron-donating strategy to guide the construction of MOF photocatalysts toward co-catalyst-free highly efficient photocatalytic H<sub>2</sub> evolution,” *Journal of Materials Chemistry and Physics*, vol. 7, no. 42, pp. 24180–24185, 2019.
- [4] F. Miao, N. Lu, P. Zhang, Z. Zhang, and G. Shao, “Multidimension-controllable synthesis of ant nest-structural electrode materials with unique 3D hierarchical porous features toward electrochemical applications,” *Advanced Functional Materials*, vol. 29, no. 29, article 1808994, 2019.
- [5] L. S. Lin, “Multifunctional Fe<sub>3</sub>O<sub>4</sub>@polydopamine core-shell nanocomposites for intracellular mRNA detection and imaging-guided photothermal therapy,” *ACS Nano*, vol. 8, no. 4, pp. 3876–3883, 2014.
- [6] M. C. Wu, A. R. Deokar, J. H. Liao, P. Y. Shih, and Y. C. Ling, “Graphene-based photothermal agent for rapid and effective killing of bacteria,” *ACS Nano*, vol. 7, no. 2, pp. 1281–1290, 2013.
- [7] K. Li, E. Hong, B. Wang et al., “Advances in the application of upconversion nanoparticles for detecting and treating cancers,” *Photodiagnosis and Photodynamic Therapy*, vol. 25, pp. 177–192, 2019.
- [8] X. Luo, Y. Wang, H. Lin, and F. Qu, “DOX-Fe<sub>3</sub>O<sub>4</sub>@mSiO<sub>2</sub>-PO-FA nanocomposite for synergistic chemo- and photothermal therapy,” *RSC Advances*, vol. 6, no. 113, pp. 112232–112240, 2016.
- [9] K. Zhang, Q. Zhao, S. Qin et al., “Nanodiamonds conjugated upconversion nanoparticles for bio-imaging and drug delivery,” *Journal of Colloid and Interface Science*, vol. 537, pp. 316–324, 2019.
- [10] A. Jędrzak, B. F. Grześkowiak, E. Coy et al., “Dendrimer based theranostic nanostructures for combined chemo- and photothermal therapy of liver cancer cells in vitro,” *Colloids and Surfaces B: Biointerfaces*, vol. 173, pp. 698–708, 2019.
- [11] X. Wang, H. Liu, D. Chen et al., “Multifunctional Fe<sub>3</sub>O<sub>4</sub>@P(St/MAA)@chitosan@Au core/shell nanoparticles for dual imaging and photothermal therapy,” *ACS Applied Materials and Interfaces*, vol. 5, no. 11, pp. 4966–4971, 2013.
- [12] M. Y. Liao, C. H. Wu, P. S. Lai et al., “Surface state mediated NIR two-photon fluorescence of iron oxides for nonlinear optical microscopy,” *Advanced Functional Materials*, vol. 23, no. 16, pp. 2044–2051, 2013.
- [13] M. E. Sadat, M. Kaveh Baghbador, A. W. Dunn et al., “Photoluminescence and photothermal effect of Fe<sub>3</sub>O<sub>4</sub> nanoparticles for medical imaging and therapy,” *Applied Physics Letters*, vol. 105, no. 9, article 091903, 2014.
- [14] L. Wu, A. Mendoza-Garcia, Q. Li, and S. Sun, “Organic phase syntheses of magnetic nanoparticles and their applications,” *Chemical Reviews*, vol. 116, no. 18, pp. 10473–10512, 2016.
- [15] Z. Wang, C. Liu, Y. Zhao et al., “Photomagnetic nanoparticles in dual-modality imaging and photo-sonodynamic activity against bacteria,” *Chemical Engineering Journal*, vol. 356, pp. 811–818, 2019.
- [16] G. Hu, N. Li, J. Tang, S. Xu, and L. Wang, “A general and facile strategy to fabricate multifunctional nanoprobe for Simultaneous 19F magnetic resonance imaging, optical/thermal imaging, and photothermal therapy,” *ACS Applied Materials and Interfaces*, vol. 8, no. 35, pp. 22830–22838, 2016.

- [17] Y. Huang, T. Wei, J. Yu, Y. Hou, K. Cai, and X. J. Liang, "Multifunctional metal rattle-type nanocarriers for MRI-guided photothermal cancer therapy," *Molecular Pharmaceutics*, vol. 11, no. 10, pp. 3386–3394, 2014.
- [18] Q. Tian, J. Hu, Y. Zhu et al., "Sub-10 nm  $\text{Fe}_3\text{O}_4@ \text{Cu}_{2-x}\text{S}$  core-shell nanoparticles for dual-modal imaging and photothermal therapy," *Journal of the American Chemical Society*, vol. 135, no. 23, pp. 8571–8577, 2013.
- [19] C. Mi, J. Zhang, H. Gao et al., "Multifunctional nanocomposites of superparamagnetic ( $\text{Fe}_3\text{O}_4$ ) and NIR-responsive rare earth-doped up-conversion fluorescent ( $\text{NaYF}_4:\text{Yb}, \text{Er}$ ) nanoparticles and their applications in biolabeling and fluorescent imaging of cancer cells," *Nanoscale*, vol. 2, no. 7, pp. 1141–1148, 2010.
- [20] D. Shi, M. E. Sadat, A. W. Dunn, and D. B. Mast, "Photo-fluorescent and magnetic properties of iron oxide nanoparticles for biomedical applications," *Nanoscale*, vol. 7, no. 18, pp. 8209–8232, 2015.
- [21] S. Shen, S. Wang, R. Zheng et al., "Magnetic nanoparticle clusters for photothermal therapy with near-infrared irradiation," *Biomaterials*, vol. 39, pp. 67–74, 2015.
- [22] P. Xue, J. Bao, Y. Wu, Y. Zhang, and Y. Kang, "Magnetic Prussian blue nanoparticles for combined enzyme-responsive drug release and photothermal therapy," *RSC Advances*, vol. 5, no. 36, pp. 28401–28409, 2015.
- [23] H. Wang, Q. Mu, R. Revia et al., "Iron oxide-carbon core-shell nanoparticles for dual-modal imaging-guided photothermal therapy," *Journal of Controlled Release*, vol. 289, pp. 70–78, 2018.
- [24] Y. Liu, Z. Zhang, Y. Fang et al., "IR-driven strong plasmonic-coupling on Ag nanorices/ $\text{W}_{18}\text{O}_{49}$  nanowires heterostructures for photo/thermal synergistic enhancement of  $\text{H}_2$  evolution from ammonia borane," *Applied Catalysis B: Environmental*, vol. 252, pp. 164–173, 2019.
- [25] L. Cheng, C. Wang, L. Feng, K. Yang, and Z. Liu, "Functional nanomaterials for phototherapies of cancer," *Chemical Reviews*, vol. 114, no. 21, pp. 10869–10939, 2014.
- [26] X. Zhang, X. Xu, T. Li et al., "Composite photothermal platform of polypyrrole-enveloped  $\text{Fe}_3\text{O}_4$  Nanoparticle self-assembled superstructures," *ACS Applied Materials and Interfaces*, vol. 6, no. 16, pp. 14552–14561, 2014.
- [27] B. Zhang, Y. Shan, and K. Chen, "A facile approach to fabricate of photothermal functional  $\text{Fe}_3\text{O}_4@ \text{CuS}$  microspheres," *Materials Chemistry and Physics*, vol. 193, pp. 82–88, 2017.
- [28] H. Wu, G. Liu, Y. Zhuang et al., "The behavior after intravenous injection in mice of multiwalled carbon nanotube/ $\text{Fe}_3\text{O}_4$  hybrid MRI contrast agents," *Biomaterials*, vol. 32, no. 21, pp. 4867–4876, 2011.
- [29] S. Sun and H. Zeng, "Size-controlled synthesis of magnetite nanoparticles," *Journal of the American Chemical Society*, vol. 124, no. 28, pp. 8204–8205, 2002.
- [30] C. M. Hessel, V. P. Pattani, M. Rasch et al., "Copper selenide nanocrystals for photothermal therapy," *Nano Lett*, vol. 11, no. 6, pp. 2560–2566, 2011.